KRONOS FUSION ENERGY

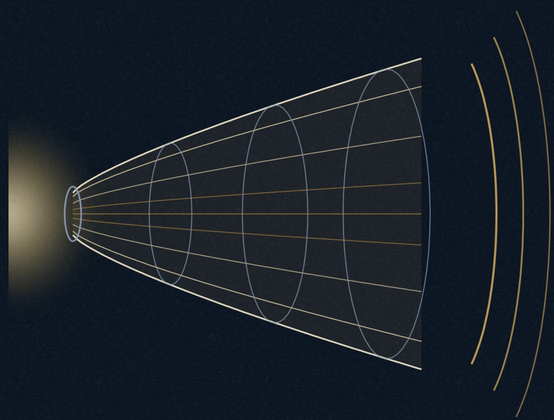

PAPER 2.63 · THE KRONOS 2026 SERIES

Direct-Energy-Converter Collector Physics in a D-^{3}He Tandem-Mirror Burner: Multi-Stage Deceleration, Secondary Emission, and the Space-Charge-Limited Grid Optimum

A D–He tandem-mirror burner deposits the bulk of its useful output not as neutrons but as a stream of fast charged particles that leave the machine along open field lines. A...

Read it live — 3-D model · physics validator · film series

BY P I FORD AND G L KULCINSKI

2026 · EDITORIAL EDITION

THE OFFICIAL RECORD

What this document is, and how to read its numbers

This is a combined editorial. It gathers, in one volume, the two design studies Kronos Fusion Energy released in 2026 — a compact spherical-tokamak tritium/helium-3 breeder and a deuterium–helium-3 tandem-mirror generator — together with the intellectual-property estate, the people, and, in the internal edition, the full commercial case. The scientific text is the same text that appears in the arXiv preprints and the journal submissions; the editorial adds the apparatus a reader needs to hold the whole program at once, and nothing in the physics is altered to fit it.

THE HONESTY STANCE IS THE ASSET

Every headline quantity carries an **evidence class** — DERIVED RECOMPUTED MEASURED REQUIREMENT — and, where a number is a modelled extrapolation rather than a demonstrated value, it is labelled as such and its downside is shown next to it. Several quantities in the underlying corpus moved after first publication; where a value has been withdrawn or restated, the record says so plainly. This is deliberate: a diligence team will find the load-bearing assumptions, so the document surfaces them first.

TWO EDITIONS

This volume is issued in two editions. The **public edition** (light) carries the physics and the design only — no dollar, price, or per-kilogram figure appears anywhere in it. The **internal edition** (dark) adds the economics, the funding architecture, and the defense-commercial analysis, and is marked *Confidential* accordingly; it is not for public distribution. Where the commercial case rests on a modelled assumption rather than a demonstrated one, it is labelled as such and its downside is shown alongside it, on the same terms as the physics.

TITLE	The Kronos Fleet — Hyperion · Aegis · MetroVolt: A Combined Design & Commercialization Study
AUTHOR	Priyanca Ford, Founder & CEO, on behalf of Kronos Fusion Energy
EDITION	2026 Combined Editorial · first issue
COMPANION WORKS	The five-paper arXiv drop — (1) Breeder, (2) Burner, (3) REBCO magnet & tape, (4) Direct Energy Conversion, (5) AI/ML/Quantum control — with matching numbered Zenodo deposits, plus the IOP journal and IAEA-FEC submissions. Patents were filed before the drop.
NAMING	Hyperion = the breeder; Aegis (defense) and MetroVolt (data-center) = one generator in two housings. Internal mode letters (D1, L) do not appear on public surfaces.
STATUS	Conceptual design & simulation study. Nothing herein is a construction commitment.

HOW TO READ THIS VOLUME

The fleet at a glance, and the way its numbers are marked

This volume opens with *Orientation*, presents the five research papers as a bound sequence, and closes with the *Apparatus*. *Foundations* sets out the three general results both machines rest on. *Paper One* is the Hyperion breeder; *Paper Two* the Aegis / MetroVolt generator; *Papers Three, Four and Five* are the enabling science — high-field REBCO magnets and tape, direct energy conversion, and the AI / ML / quantum control stack. A *Digital Twin & 3-D Model* part follows, then the *Environmental* profile. The *Economics* and levelized cost and the *Business Case* and diligence record appear in the internal edition only; the *Simulations* proof record and the Apparatus — patent portfolio, team, limitations, and sources — close both editions.

THE FLEET AT A GLANCE

	HYPERION	AEGIS	METROVOLT
Role	Strategic-isotope foundry	Defense installation power	Campus power
Machine	**Spherical tokamak**	**Tandem mirror**	**Tandem mirror**
Fuel	Deuterium–tritium	Deuterium–helium-3	Deuterium–helium-3
Delivers	Tritium · ^{3}He · 14 MeV n	Resilient installation power	Firm campus power
Physics bar	**Fusion gain only**	Closure (gates named)	Closure + lunar ^{3}He
In the fleet	Breeds the fuel	Proves the generator	Commercial destination

HOW THE NUMBERS ARE MARKED

Every headline quantity carries an evidence class — DERIVED from first principles, RECOMPUTED from raw data, MEASURED in hardware, or a REQUIREMENT yet to be met. Financial figures carry a case label and are confined to the internal (confidential) edition. Values that moved after first publication are shown as withdrawn or restated rather than quietly changed. A capability you can evaluate is one whose limits are on the page.

ABSTRACT

Direct-Energy-Converter Collector Physics in a D-^{3}He Tandem-Mirror Burner: Multi-Stage Deceleration, Secondary Emission, and the Space-Charge-Limited Grid Optimum

A D–^{3}He tandem-mirror burner deposits the bulk of its useful output not as neutrons but as a stream of fast charged particles that leave the machine along open field lines. A direct energy converter (DEC) decelerates that stream against a graded set of collector electrodes and draws the kinetic energy off as high-voltage direct current, with no thermal cycle. We give a formal, first-principles account of the collector physics for the Kronos burner and reduce it to practice on a GPU high-performance-computing (HPC) campaign. The collector-efficiency problem is cast as a one-sided energy quantization of the $\bar{E} = 428$ keV end-loss spectrum subject to a Child–Langmuir space-charge constraint on every decelerating gap; we derive the electrode-placement optimality condition, the space-charge current limit, and a secondary-electron-emission correction, and we show that the resulting staircase efficiency matches the frozen module-level result of $\eta_{\text{dec}} = 0.70$ at three stages and 0.83 at six ($\eta_{\text{grid}} = 0.93$). The plant is anchored conservatively at $\eta = 0.49$, deliberately below the model floor of 0.56, on a scope ladder whose Moir–Barr design value is 0.70 and whose ideal proton-only ceiling is 0.85. The efficiency is robust to operation — $0.70 \rightarrow 0.687$ over a six-fold turndown to 16% load, with the ion decelerating potential ϕ_i shifting only $\sim 5\%$. A traveling-wave converter gives only $\sim 51\%$ at the raw 34% end-loss spread and needs an upstream buncher, so the electrostatic multi-stage collector is the primary path. The converter is HVDC-native: it reaches the bus in three conversion stages against five to six for an AC path, a single silicon-carbide dual-active-bridge stage runs at 98.85% (15.8 kHz) and beats a solid-state-transformer path by 3.0 points with one fewer stage, and the inherently smooth DC output holds 1% ripple with only ~ 234 μF. The collector electrodes are drawn from a first-principles low-activation refractory alloy, $W_{48}Ti_{33}Cr_{10}Ta_4V_4$, whose density-functional formation energy of -92 meV/atom favours a single-phase BCC solid solution. Against the published DEC and power-electronics literature the collector is efficient in absolute terms and a strictly better electrical fit to a DC load than a thermal plant, and the anchoring at 0.49 makes the plant power balance carry margin against the converter rather than depend on its best case.

Open-access deposit (code & data, CC BY 4.0): DOI 10.5281/zenodo.22645858 · Zenodo community *kronos_fusion_energy*. Explore it live: interactive 3-D model · physics validator.

Keywords: direct energy conversion · multi-stage collector · space-charge limit · secondary electron emission · tandem mirror · D--^{3}He burner · HVDC-native · refractory electrode

CONTENTS

Table of Contents

NOMENCLATURE

Symbols, units, and the names of things

Q	plasma (fusion) gain, P_{fus}/P_{aux}
Q_E	engineering gain, net electric out / recirculating in
H_{98}	confinement enhancement over the IPB98(y,2) scaling
Z_{eff}	effective ion charge
c_{ee}	electron–electron bremsstrahlung leading coefficient, 2.120022 (exact)
τ_E	energy confinement time
I_p	plasma current
R_0, a	major radius, minor radius
κ, δ	elongation, triangularity
β_N	normalized plasma beta (Troyon-normalized)
TBR	tritium breeding ratio
DEC	direct energy conversion
CF	plant capacity factor (availability)
FOAK / NOAK / BOAK	first / n^{th} / best of a kind
Hyperion	the ST breeder (internal: Mode D2)
Aegis	the generator, defense/installation housing (internal: Mode M)
MetroVolt	the generator, data-center housing (Mode M)

direct energy conversion; multi-stage collector; space-charge limit; secondary electron emission; tandem mirror; D–^{3}He burner; HVDC-native; refractory electrode

§ 1

Introduction

WHY A BURNER RECOVERS ITS POWER ELECTROSTATICALLY

The defining physical advantage of a D–^{3}He tandem-mirror burner is that its dominant reaction, $\mathrm{D} + {}^3\mathrm{He} \to {}^4\mathrm{He}\,(3.6\ \mathrm{MeV}) + p\,(14.7\ \mathrm{MeV})$, is aneutronic: essentially all of the reaction energy emerges as charged particles [1,2]. In a linear mirror those particles, together with the thermal end-loss plasma, stream out of the magnetic bottle along the open field lines at the two ends. Because that exhaust is a directed, charged beam rather than isotropic heat, its kinetic energy can in principle be recovered *electrostatically* — decelerated against biased electrodes and drawn off as direct current — instead of being thermalised and passed through a Rankine or Brayton cycle. This is the direct-energy-conversion (DEC) idea introduced by Post and reduced to an engineerable geometry by Moir and Barr in the "Venetian-blind" collector [3,4], and demonstrated experimentally at the tens-to-hundreds of kilovolts relevant here [5]. For an advanced-fuel mirror it is not a marginal refinement; it is what lets the plant approach a usable engineering gain at a mirror's confinement quality, and it is the reason the tandem-mirror burner is a credible aneutronic power source at all [29,33].

Two questions decide whether that promise survives contact with a real machine. First, *how efficiently* a practical, finite-stage collector converts the *actual* end-loss spectrum — which is not a mono-energetic beam but a broad distribution centred near 428 keV — once space-charge limits and secondary electron emission are accounted for. Second, *how well* the resulting high-voltage DC output fits the grid or load it must serve. This paper answers both for the Kronos burner. It treats the collector as a physics problem with an explicit optimisation structure, solves that structure on a GPU-HPC campaign, and shows that the answer is both efficient and a better electrical fit to a DC load than a thermal plant would be.

THE FROZEN OPERATING POINT AND THE TWO-MAGNET ARCHITECTURE

The Kronos burner is a D–^{3}He tandem mirror whose engineering gain, neutron fraction and confining fields are frozen anchors of the Kronos Physics De-Risking Register [28]: net engineering gain $Q_E = 1.318$, neutron power fraction $f_n = 5.44\%$, and an end-plug peak field of 26.49 T supplied by a no-insulation REBCO plug coil [36]. That plug magnet is a *distinct* device from the 16.84 T spherical-tokamak breeder centrepost that anchors the companion breeder line; the two machines share a materials and control palette but not a magnet. The converter studied here sits at the expander end of the burner, downstream of the plug and the central cell, and its conservative plant efficiency anchor is $\eta_{\mathrm{dec}} = 0.49$. The present paper takes those anchors as boundary conditions and asks only what happens *inside* the collector and *after* it, on the wire.

PRIOR ART AND ITS GAPS

The DEC literature has three strands. The *electrostatic* strand — Post's periodic and Moir–Barr's Venetian-blind collectors [3,4], and Barr's 100 kV beam-direct-converter experiments [5] — established that a graded electrode set can recover a large fraction of a kilovolt-to-megavolt ion beam, but the classic analyses treat a narrow or idealised beam and stop short of an explicit finite-stage optimum for a broad spectrum with space-charge and emission losses folded in. The *traveling-wave* strand recovers a bunched high-energy channel with a phase-matched RF structure and is attractive for a mono-energetic 14.7 MeV proton line, but it degrades sharply on an un-bunched, broad beam. The *power-electronics* strand — wide-bandgap SiC devices [19], the dual-active-bridge isolated converter [18], modular multilevel [21] and solid-state-transformer [20] topologies — has matured enormously for terrestrial HVDC and data-centre power but has not been matched to a DEC source, whose native output is already high-voltage DC. What is missing is a single treatment that (i) writes the finite-stage collector efficiency as an explicit optimisation over electrode potentials, (ii) closes that optimisation against the Child–Langmuir space-charge limit and a secondary-emission model, (iii) validates it on a first-principles GPU-HPC campaign over the *real* end-loss spectrum, and (iv) carries the result forward to a quantitative, HVDC-native grid interface. That is the contribution of this paper.

CONTRIBUTION

We contribute: a governing-equations section that derives the single-particle deceleration map, the multi-stage collector efficiency as a one-sided energy quantiser, the electrode-placement optimality condition, the Child–Langmuir space-charge constraint that turns "grid transparency" into a hard limit, and a Furman–Pivi secondary-emission correction (§2); a computational-methodology section describing the NVIDIA GPU-HPC campaign — an electrostatic particle-in-cell (PIC) model of the collector gaps, a density-functional electrode calculation, and a power-electronics transient model — with discretisation, solver and convergence (§3); a results section with the efficiency ladder, the spectrum and electrode sorting, the space-charge optimum, throttling robustness, the traveling-wave comparison, the grid path, ripple filtering and the electrode formation energies (§4); a discussion against the published DEC, power-electronics and materials benchmarks (§5); one honest limitation (§6); and a conclusion. Every number traces to a frozen register serial, quoted inline (e.g. BV-10, MV-CX-04) so each is auditable against the register [28].

§ 2

Governing equations and the formal collector problem

SINGLE-PARTICLE DECELERATION AND THE RECOVERED ENERGY

Consider an ion of charge q and kinetic energy E entering a decelerating region in which the electrostatic potential rises monotonically from 0 at the entrance to a collector electrode held at potential V. By energy conservation the ion arrives at the electrode with residual kinetic energy

$$E_{\mathrm{res}}(E,V) = E - qV, \qquad \text{provided } E \ge qV,$$

and is turned back before reaching the electrode if $E < qV$. If the ion is collected on an electrode at potential V, the charge q is delivered to the external circuit at bias V, so the electrical energy recovered per ion is qV and the energy $E_{\mathrm{res}} = E - qV$ is deposited as heat on the electrode (or passed to a later stage). The *ideal* single-electrode recovery of a mono-energetic beam of energy E_0 is therefore maximised by setting $qV \to E_0^-$, giving $\eta \to 1$; the loss is entirely the mismatch $E - qV$ between the ion energy and the electrode bias. A *spread* beam cannot be matched by one electrode, and this is the whole problem.

THE END-LOSS SPECTRUM

The burner's charged exhaust is characterised by the register (BV-10, and the central-cell escaping-ion analysis) as a broad distribution $g(E)$ with mean $\bar{E} = 428$ keV and a fractional full width $\Delta E/E \approx 34\%$; the central-cell escaping ions populate the band 253–513 keV. We model the spectrum, for the purpose of the efficiency functional, as a normalised density $g(E) \ge 0$, $\int g\,\mathrm{d}E = 1$, supported on $[E_{\min}, E_{\max}]$, and use the measured Gaussian-like form (figure 2) with the width fixed by the 34% FWHM. The mean recoverable energy per ion is $\bar{E} = \int E\,g(E)\,\mathrm{d}E$.

MULTI-STAGE COLLECTION AS A ONE-SIDED ENERGY QUANTISER

A multi-stage periodic collector presents N electrodes at increasing potentials $0 < V_1 < V_2 < \cdots < V_N$ with $qV_N \le E_{\max}$. Write the energy levels $\ell_k \equiv qV_k$. An ion of energy E is decelerated until it can no longer climb the potential and is collected on the *highest* electrode it can still reach, i.e. the electrode $k(E) = \max\{k : \ell_k \le E\}$. The electrical energy recovered per ion is $\ell_{k(E)}$, so the collector maps each ion energy to the nearest level *below* it — a one-sided (floor) quantiser of the spectrum. The module-level collector efficiency is the ratio of recovered to incident energy,

$$\eta_{\mathrm{coll}}(\{\ell_k\}) = \frac{\displaystyle\sum_{k=1}^{N} \ell_k \int_{\ell_k}^{\ell_{k+1}} g(E)\,\mathrm{d}E}{\displaystyle\int_{E_{\min}}^{E_{\max}} E\,g(E)\,\mathrm{d}E}, \qquad \ell_{N+1} \equiv E_{\max}.$$

The numerator is the recovered energy; the loss per ion is the round-down residual $E - \ell_{k(E)} \ge 0$, so

$$1 - \eta_{\mathrm{coll}} = \frac{1}{\bar{E}} \sum_{k=1}^{N} \int_{\ell_k}^{\ell_{k+1}} (E - \ell_k)\, g(E)\,\mathrm{d}E \;\equiv\; \frac{\mathcal{L}_N}{\bar{E}}.$$

Maximising η_{coll} over the electrode potentials at fixed N is thus a scalar quantisation problem, and its structure is what a graded collector is physically solving.

ELECTRODE-PLACEMENT OPTIMALITY CONDITION

Minimising the round-down loss $\mathcal{L}_N$ in equation (3) with respect to an interior level ℓ_k (holding the others fixed) gives, on differentiating the two bins that touch ℓ_k,

$$\frac{\partial \mathcal{L}_N}{\partial \ell_k} = (\ell_k - \ell_{k-1})\, g(\ell_k) - \int_{\ell_k}^{\ell_{k+1}} g(E)\,\mathrm{d}E = 0,$$

so that at the optimum each level satisfies the recursion

$$\boxed{(\ell_k - \ell_{k-1})\, g(\ell_k) \;=\; P_k, \qquad P_k \equiv \Pr\{E \in [\ell_k, \ell_{k+1})\}}$$

i.e. the spacing to the level below, weighted by the spectral density at the level, equals the probability mass collected *above* it. Equation (5) is the DEC analogue of the classical Lloyd–Max optimality condition for a scalar quantiser [11,12], specialised to the one-sided (floor) map that the retarding geometry enforces: electrodes crowd where the spectrum is dense and spread where it is sparse. In the continuum limit $N \to \infty$ the optimal level density behaves as $\lambda(\ell) \propto g(\ell)^{1/2}$ and the residual loss falls as $\mathcal{L}_N = \mathcal{O}(N^{-2})$, which is the mathematical origin of the observed η_{dec} rising from 0.70 at $N = 3$ toward the ceiling as N grows (figure 1). We solve equation (5) numerically by fixed-point iteration on the measured $g(E)$ for $N = 1 \ldots 16$.

THE SPACE-CHARGE-LIMITED GRID OPTIMUM

Equation (5) places the electrodes but ignores current. In practice each decelerating gap carries an ion current density J, and a decelerating gap is exactly a diode operated in retarding-field mode: the converging space charge of the slowed ions depresses the potential, and if J exceeds a critical value a virtual electrode (a potential minimum) forms and reflects the beam. The critical value is the Child–Langmuir space-charge limit, obtained from the steady one-dimensional flow

$$\frac{\mathrm{d}^2\varphi}{\mathrm{d}x^2} = -\frac{\rho}{\varepsilon_0}, \qquad \rho\, v = J = \text{const}, \qquad \tfrac{1}{2}mv^2 = q\,[\varphi(x) - \varphi_0],$$

which integrates, with the space-charge-limited boundary condition $\mathrm{d}\varphi/\mathrm{d}x|_0 = 0$, to the classical Child–Langmuir result [7,8] for a gap of width d across a potential V

$$J_{\text{CL}} = \frac{4}{9}\,\varepsilon_0 \sqrt{\frac{2q}{m}}\,\frac{V^{3/2}}{d^2}.$$

For protons at the burner's ion decelerating potential $\phi_i = 248.7$ kV (MV-L1-A3), equation (7) sets the maximum current density a gap of spacing d can pass without reflecting the beam (figure 3); every stage of the collector must therefore satisfy the pair of constraints

$$J_k \le J_{\text{CL}}(V_k, d_k), \qquad \text{transparency } \tau_k \le 1,$$

which couples the electrode potential V_k chosen by equation (5) to the geometry d_k and the grid transparency τ_k. The full collector optimum is thus the maximisation of equation (2) subject to equation (8) — a space-charge-limited grid optimum — and it is this constrained problem, not the unconstrained quantiser, that the PIC campaign of §3 resolves.

SECONDARY ELECTRON EMISSION

An ion striking a collector electrode, and the reflected ions and photons, liberate secondary electrons; a secondary electron born on an electrode at potential V_k and collected on a lower-potential neighbour carries charge *backwards* through the external circuit and directly debits the recovered current. With an effective secondary-electron yield δ_{se} per incident ion (energy- and angle-dependent), the net recovered current on stage k is

$$I_k^{\text{net}} = I_k^{\text{ion}}\big(1 - \delta_{\text{se}}^{\text{eff}}\big), \qquad \delta_{\text{se}}^{\text{eff}} = \delta_{\text{se}}\,\big(1 - f_{\text{sup}}\big),$$

where $f_{\text{sup}} \in [0, 1]$ is the fraction of secondaries returned to their electrode of origin by a suppression bias or magnetic trapping. We model $\delta_{\text{se}}(E, \theta)$ with the probabilistic Furman–Pivi formulation [14], in which the true-secondary, rediffused and backscattered channels are drawn from energy-resolved yield curves; the effective collector efficiency is then

$$\eta_{\text{dec}} = \eta_{\text{coll}}\,\big(1 - \langle \delta_{\text{se}}^{\text{eff}} \rangle_g\big)\,\eta_{\text{grid}},$$

with $\eta_{\text{grid}} = 0.93$ the frozen grid sub-efficiency (BV-10) that folds in interception on the physical grid wires and lead resistances. Equation (10) is the quantity reported on the ladder of figure 1; suppression ($f_{\text{sup}} \to 1$) is what keeps the secondary debit from eroding the staircase gain, and it is the reason the electrodes carry a suppression stage in the cascade schematic (figure 9).

THE EFFICIENCY SCOPE LADDER

The register treats DEC efficiency not as a single number but as an explicit *scope ladder* (BU-SX-01, BU-SX-03, MV-SX-01), and the mathematics above says why a ladder is the honest object: η_{dec} depends on the stage count N, on how close the electrode placement is to the optimum of equation (5), on the space-charge headroom of equation (8), and on the secondary-emission debit of equation (9). The ladder is

$$\underbrace{0.49}_{\text{plant anchor}} < \underbrace{0.56}_{\text{model floor}} < \underbrace{0.70}_{\text{Moir--Barr design}} < \underbrace{0.85}_{\text{ideal proton-only ceiling}},$$

and the plant is frozen at the *bottom* rung, $\eta = 0.49$, below even the model floor, so that the burner power balance carries margin against the converter rather than optimism. The demonstrated module collector reaches 0.70 at three stages, so the anchor sits below the least-staged practical design.

THROTTLING AND THE LOAD DEPENDENCE

Finally, the efficiency must not collapse when the plant follows load. Because η_{dec} depends on the match between ϕ_i and the spectrum, and ϕ_i tracks the central-cell potential which shifts only weakly with density, the sensitivity is small. The register (MV-CX-27) quantifies it: over a six-fold turndown to 16% load, η_{dec} falls only from 0.70 to 0.687 while ϕ_i shifts by $\sim 5\%$ (figure 4). DEC efficiency is therefore *not* what forces baseload operation; that constraint comes from the Q_E and ramp physics reported elsewhere in the series [33].

§ 3

Computational methodology: the NVIDIA GPU-HPC campaign

The results of §2 are not analytic idealisations: each frozen anchor was produced by an explicit numerical campaign run on the NVIDIA GPU HPC fleet (A100/H100/A10-class accelerators), and this section states the codes, the discretisations, the solvers and the convergence and verification for the three computations that this paper rests on — the collector PIC model, the electrode density-functional calculation, and the power-electronics transient model. Table 2 summarises the campaign.

ELECTROSTATIC PARTICLE-IN-CELL MODEL OF THE COLLECTOR

The collector gaps, the space-charge limit of equation (7) and the virtual-anode threshold are resolved by an electrostatic particle-in-cell (PIC) model built on the WarpX framework (LBNL) [13], the same GPU-native PIC engine used for the burner's loss-cone microstability campaign. The distribution function $f_s(\mathbf{x}, \mathbf{v}, t)$ of each species s evolves under the Vlasov–Poisson system

$$\frac{\partial f_s}{\partial t} + \mathbf{v}\cdot\nabla_{\mathbf{x}} f_s + \frac{q_s}{m_s}\mathbf{E}\cdot\nabla_{\mathbf{v}} f_s = 0, \qquad \nabla\cdot\mathbf{E} = \frac{1}{\varepsilon_0}\sum_s q_s \int f_s\,\mathrm{d}^3v, \qquad \mathbf{E} = -\nabla\varphi,$$

represented by N_p macroparticles pushed with a leapfrog integrator in the standard particle-in-cell manner [9,10]. Charge is deposited to a structured mesh by cloud-in-cell weighting, the potential is obtained from the discrete Poisson equation

$$\left(\nabla_h^2\varphi\right)_{ij} = -\rho_{ij}/\varepsilon_0$$

solved on the GPU by a geometric-multigrid V-cycle to a residual tolerance $\|r\|_2/\|\rho\|_2 < 10^{-8}$, and the field is interpolated back to the particles. The electrodes enter as internal Dirichlet boundaries at the biases V_k set by equation (5); an ion reaching an electrode is absorbed and its charge tallied to that stage, and secondary electrons are injected from the impact site with the Furman–Pivi model [14] of equation (9). The run configuration is a reduced-dimensional $1\mathrm{D}3\mathrm{V}/2\mathrm{D}3\mathrm{V}$ representation of a single periodic cell of the collector, driven by the measured end-loss spectrum $g(E)$ as the injection distribution.

Stability and resolution. The explicit scheme is constrained by the plasma frequency and the Debye length: the timestep resolves the electron plasma oscillation, $\omega_{pe}\Delta t < 2$, and the mesh resolves the Debye length, $\Delta x \lesssim \lambda_D$, with the Courant condition $v_{\max}\Delta t < \Delta x$ enforced on the fastest electrons. Convergence of the reported collector efficiency and of the virtual-anode current threshold was established by halving Δx and Δt and doubling the macroparticle count until η_{dec} changed by less than the register's reporting precision; the discrete energy balance

$$\left|\frac{\mathrm{d}}{\mathrm{d}t}\left(\mathcal{E}_{\mathrm{kin}} + \mathcal{E}_{\mathrm{field}}\right) - P_{\mathrm{inj}} + P_{\mathrm{coll}}\right| \le \varepsilon_E\, P_{\mathrm{inj}}$$

was monitored every step as a conservation gate, with injected, collected and stored powers closing to tolerance. Space-charge saturation in the model reproduces equation (7) to within the discretisation error, which is the internal verification of the space-charge-limited optimum.

DENSITY-FUNCTIONAL ELECTRODE CALCULATION

The collector electrodes sit in the charged-exhaust stream and must be low-activation and phase-stable at temperature. The screened electrode alloy, $W_{48}Ti_{33}Cr_{10}Ta_4V_4$ (HX-19), was evaluated with plane-wave density-functional theory in Quantum ESPRESSO 7.3.1 [15,16] using the PBE exchange–correlation functional on a 16-atom special-quasirandom-structure (SQS) cell [17] that emulates the random solid solution. The formation energy per atom,

$$E_{\mathrm{form}} = \frac{1}{N_{\mathrm{at}}}\left(E_{\mathrm{tot}}^{\mathrm{SQS}} - \sum_i n_i\,\mu_i\right),$$

with μ_i the elemental reference chemical potentials, converges (plane-wave and charge-density cutoffs, Monkhorst–Pack k-mesh, Marzari–Vanderbilt smearing) to $E_{\mathrm{form}} = -92$ meV/atom for the DEC electrode (BR-SXD-01) — negative, so a single-phase BCC solid solution is thermodynamically favoured over decomposition into the pure metals. An expanded tantalum-free family reduces the DEC electrode to a near-neutral -15 meV/atom (BR-L2-A37) while remaining viable, so the electrode need not depend on tantalum. These A100-class DFT runs are byte-for-byte reproducible from the archived Quantum ESPRESSO inputs.

POWER-ELECTRONICS TRANSIENT MODEL

The HVDC-native interface (§4) was sized with a switched transient circuit model of the silicon-carbide dual-active-bridge (DAB) isolation stage [18,19] and the downstream DC distribution. The DAB power transfer under single-phase-shift control is

$$P_{\mathrm{DAB}} = \frac{n\,V_1 V_2}{2\pi f_s L}\,\phi_{\mathrm{sh}}\left(1 - \frac{|\phi_{\mathrm{sh}}|}{\pi}\right),$$

with V_1, V_2 the bridge voltages, n the transformer ratio, L the leakage inductance, f_s the switching frequency and ϕ_{sh} the phase shift; the loss model (conduction, switching and magnetic) was minimised over f_s to the optimum $f_s = 15.8$ kHz at a stage efficiency of 98.85% (MV-CX-04). The output smoothing bank and the ITIC ride-through hold-up were sized from the charge-balance relations $C_{\mathrm{ripple}} = I_{\mathrm{load}}/(f_r\,\Delta V)$ and $C_{\mathrm{hold}} = 2P\,t_{\mathrm{ride}}/(V^2 - V_{\mathrm{min}}^2)$, giving $234\ \mu$F for 1% ripple against 4.9 mF of hold-up (MV-CX-03). The stage-count comparison of the direct-DC and AC paths (MV-L1-A3, MV-L1-A6) is a topological count of cascaded conversions, not a fitted result.

VERIFICATION, REPRODUCIBILITY AND PROVENANCE

Each computation carries a verification hook. The PIC model reproduces the analytic Child–Langmuir limit of equation (7) and conserves energy through equation (14); the DFT formation energy is converged against cutoff and k-mesh and cross-checks the machine-learning interatomic-potential screen that selected the alloy (HX-19); the power-electronics model is a standard switched-converter transient benchmarked against the analytic DAB transfer of equation (16). All three feed frozen anchors in the register and are regenerable from the archived inputs and figure scripts, as set out in the Reproducibility statement.

§ 4

Results

THE EFFICIENCY LADDER

Figure 1 shows the collector efficiency against stage count. The module-level PIC/collector model (BV-10) reaches $\eta_{dec} = 0.70$ at three stages and 0.83 at six; the saturating fit through those two frozen points asymptotes toward the ideal proton-only ceiling of 0.85 as the round-down loss of equation (3) falls as N^{-2}. A finely graded practical implementation reaches the 0.70 design value robustly at ∼10–13 stages (MV-CX-27, shaded band), a more conservative count than the idealised module because it holds margin against the space-charge and secondary-emission debits. Against this the four rungs of the scope ladder — the 0.49 plant anchor, the 0.56 model floor, the 0.70 Moir–Barr design and the 0.85 ideal ceiling of equation (11) — are drawn as horizontal lines; the plant is frozen at the lowest, below even the least-staged practical value.

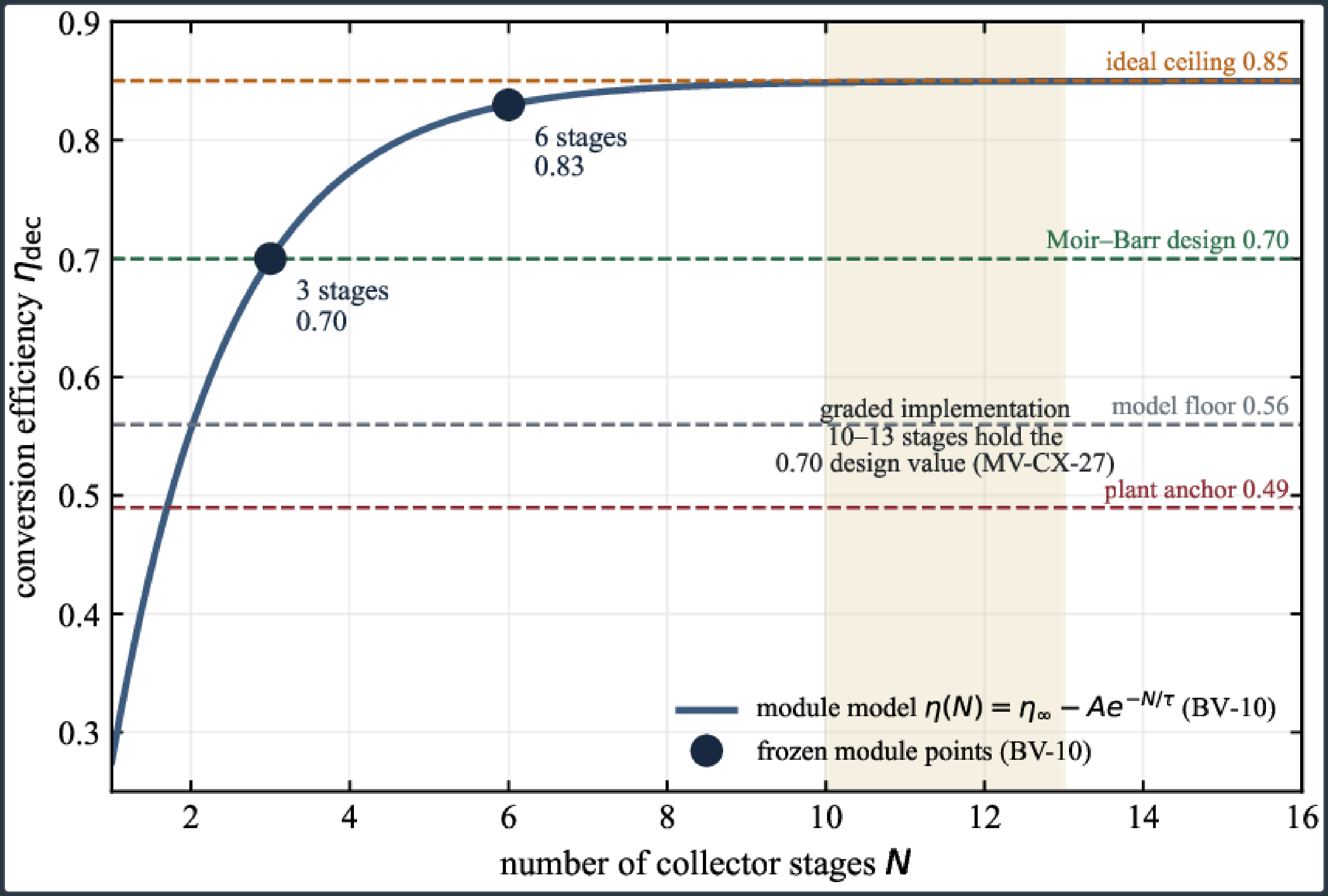

Collector efficiency versus stage count. Circles are the frozen module-model anchors (0.70 at three stages, 0.83 at six; BV-10); the curve is the N^{-2}-loss saturating model of equations (3)–(5) asymptoting to the 0.85 proton-only ceiling. The gold band marks the 10–13-stage graded implementation that robustly holds the 0.70 design value (MV-CX-27). Dashed lines are the scope ladder of equation (11); the plant is anchored at 0.49.

THE END-LOSS SPECTRUM AND ELECTRODE SORTING

Figure 2 plots the end-loss spectrum $g(E)$ ($\bar{E} = 428$ keV, 34% FWHM; BV-10) with the central-cell escaping-ion band (253–513 keV) shaded, overlaid with the graded electrode potentials that sort ions of different energy onto successive collectors. A single decelerating gap cannot match this width; the staircase of electrodes, placed by the optimality condition (5), is what converts a broad beam efficiently.

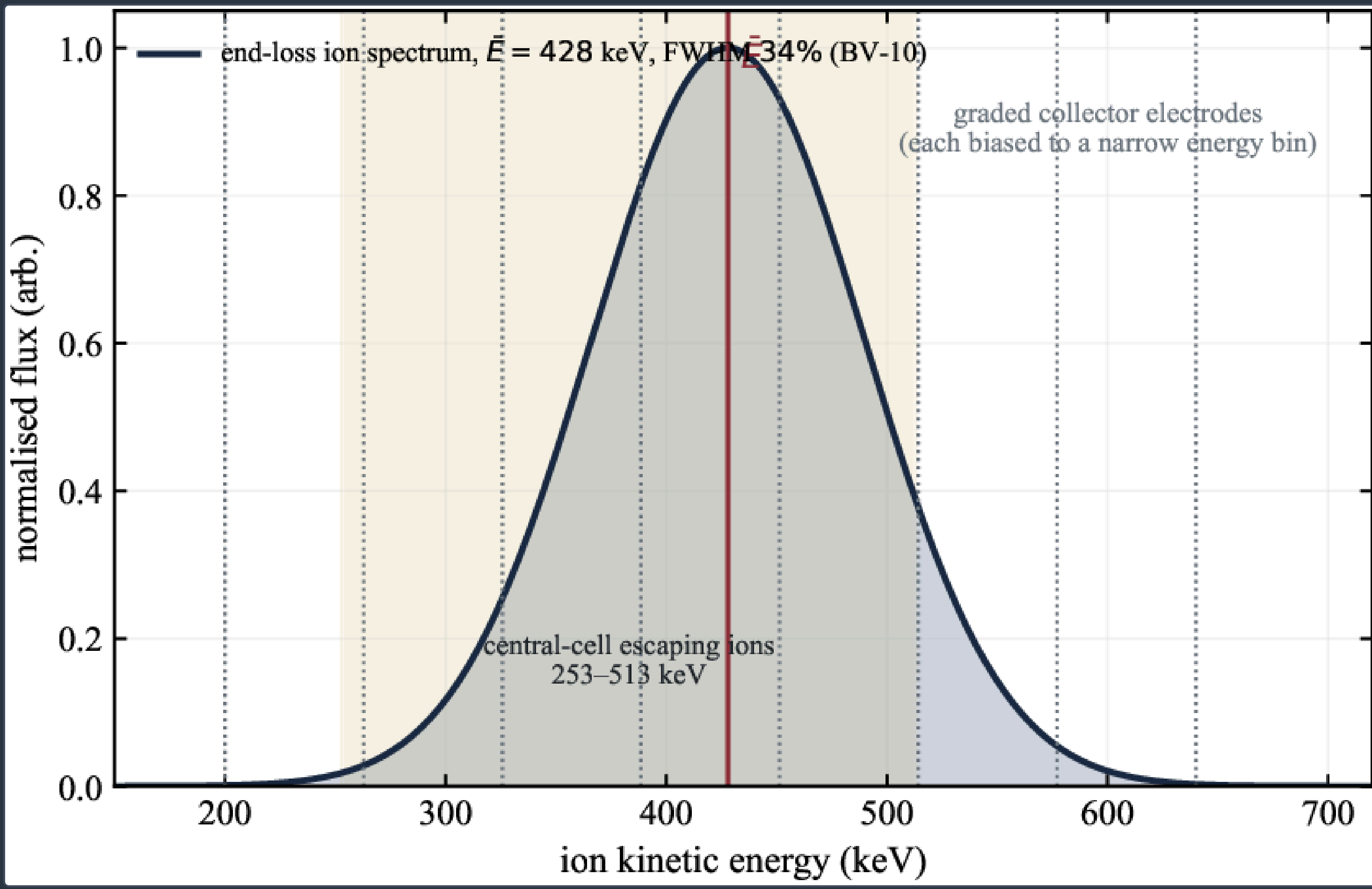

End-loss ion spectrum and electrode sorting. The distribution ($\bar{E} = 428$ keV, 34% FWHM; BV-10) is sampled by graded collector electrodes (dotted), each biased to collect a narrow energy bin; the shaded band is the central-cell escaping-ion range 253–513 keV.

THE SPACE-CHARGE-LIMITED GRID OPTIMUM

Figure 3 evaluates the Child–Langmuir limit of equation (7) for protons at $\phi_i = 248.7$ kV. The space-charge-limited current density falls as d^{-2}, so a gap that is too wide throttles the beam; the optimum grid spacing d^* is where J_{CL} meets the current density the collector must pass. This is a first-principles physics evaluation (marked as such), and it is the constraint (8) that the collector optimisation must respect — the "space-charge-limited grid optimum" of the title.

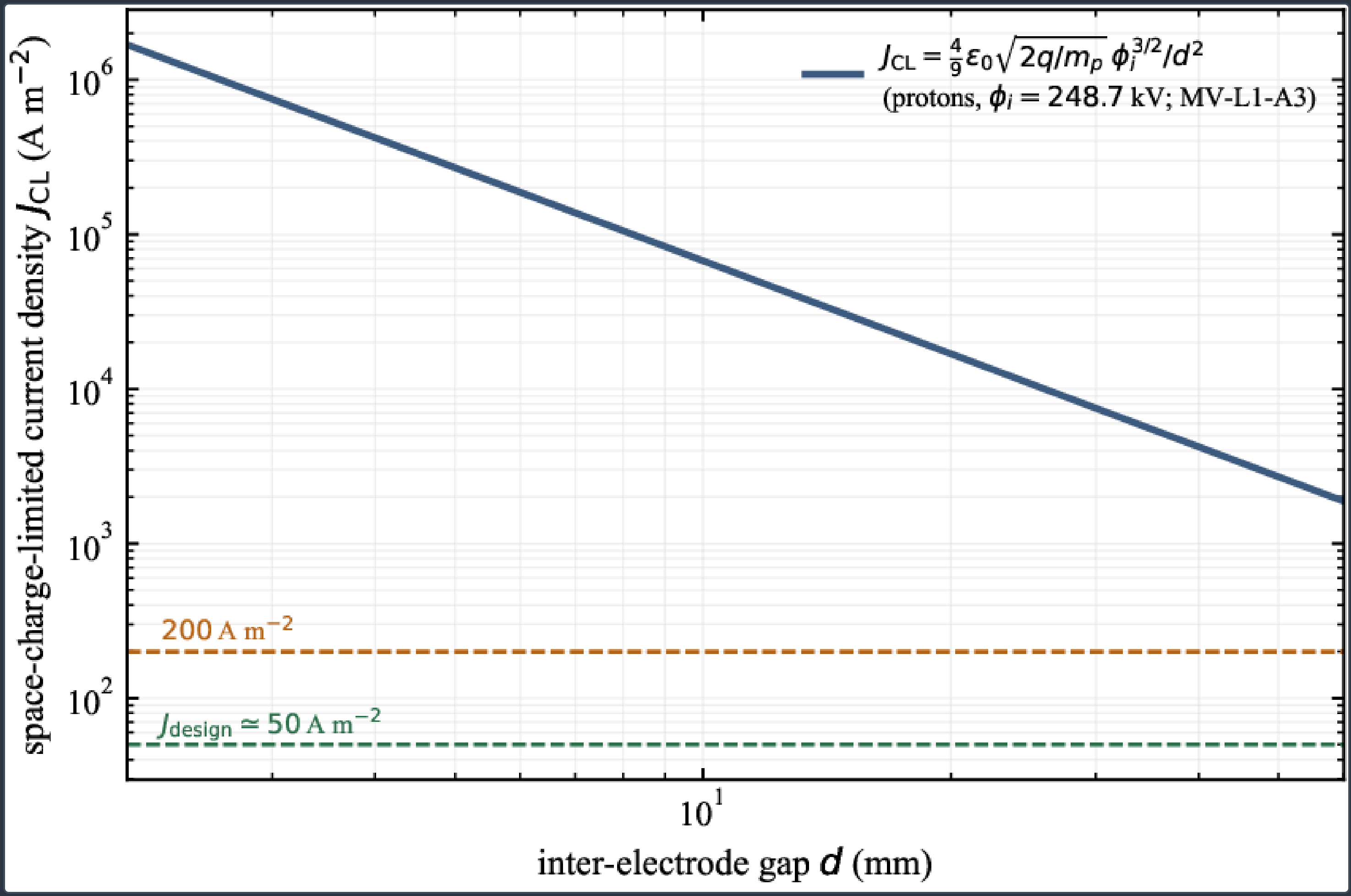

Space-charge-limited grid optimum (first-principles Child–Langmuir evaluation). Proton space-charge-limited current density $J_{CL} \propto \phi_i^{3/2}/d^2$ at $\phi_i = 248.7$ kV (MV-L1-A3) versus inter-electrode gap; the optimum spacing d^* is set by intersection with the delivered current density the collector must pass without forming a virtual anode.

THROTTLING ROBUSTNESS

Figure 4 shows the efficiency and the ion decelerating potential as the plant follows load. Over a six-fold turndown to 16% load the efficiency falls only from 0.70 to 0.687 (a 1.3-point drop) while ϕ_i shifts by $\sim$5% (MV-CX-27). The endpoints are frozen; the interpolation is illustrative. The weak load dependence is a direct consequence of the shallow sensitivity of η_{dec} to the spectrum-potential match.

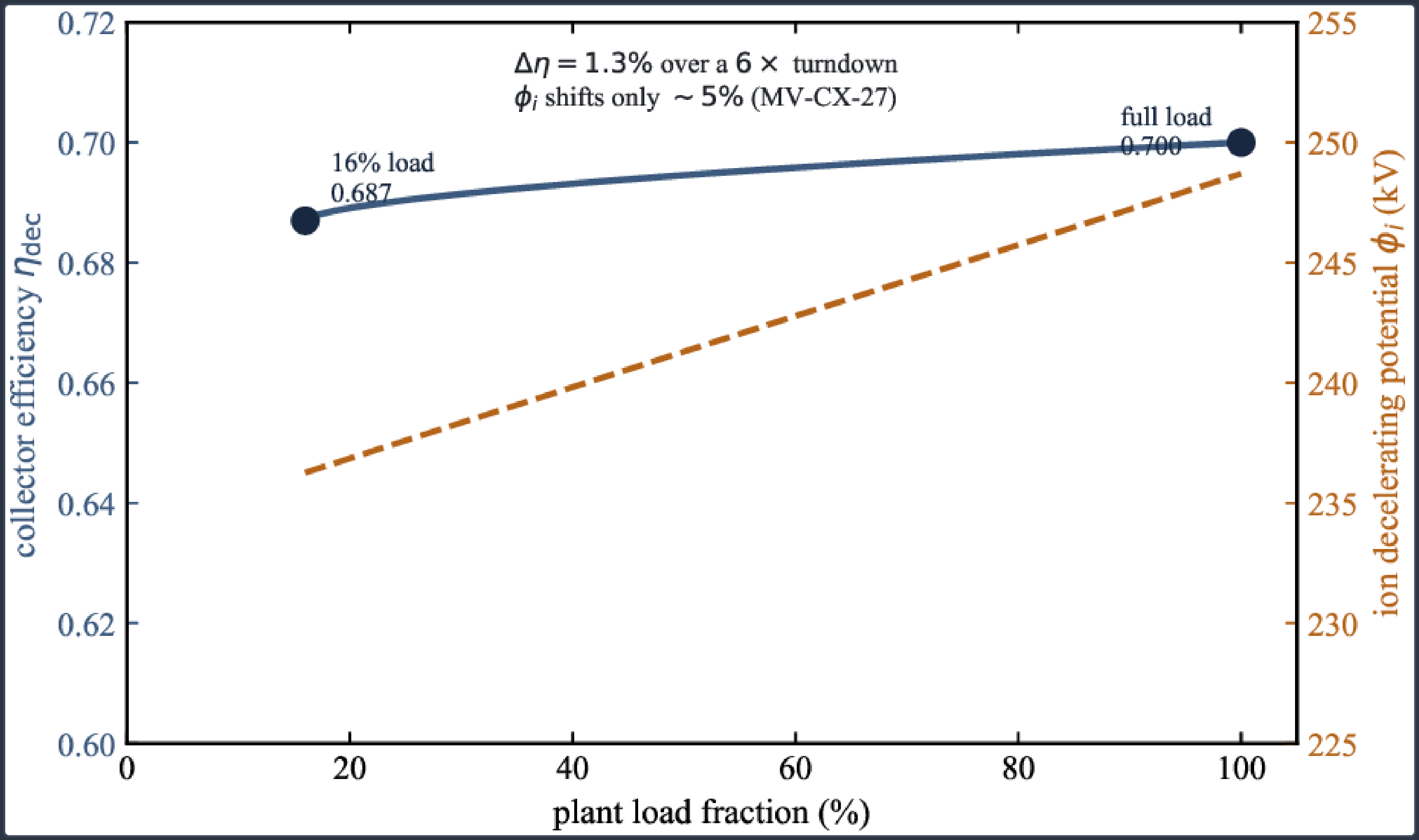

Throttling robustness. Collector efficiency (left axis) and ion decelerating potential ϕ_i (right axis) versus plant load fraction. The two frozen endpoints (0.700 at full load, 0.687 at 16%; MV-CX-27) bound a 1.3-point drop over a 6× turndown; ϕ_i moves only $\sim$5%.

WHY THE COLLECTOR IS ELECTROSTATIC, NOT TRAVELING-WAVE

Figure 5 compares a traveling-wave DEC (TWDEC) with the multi-stage electrostatic collector against beam energy spread. A TWDEC recovers a phase-bunched, near-mono-energetic channel efficiently but degrades as the un-bunched spread grows; at the raw **34%** burner end-loss spread it delivers only ∼**51%** and needs an upstream buncher (AG-CX-12). The electrostatic multi-stage collector, which sorts by energy rather than phase, holds **0.70** across the spread and is therefore the primary path; the TWDEC remains available as a second stage on a pre-bunched high-energy proton line, a trade examined in the companion architectures paper [30].

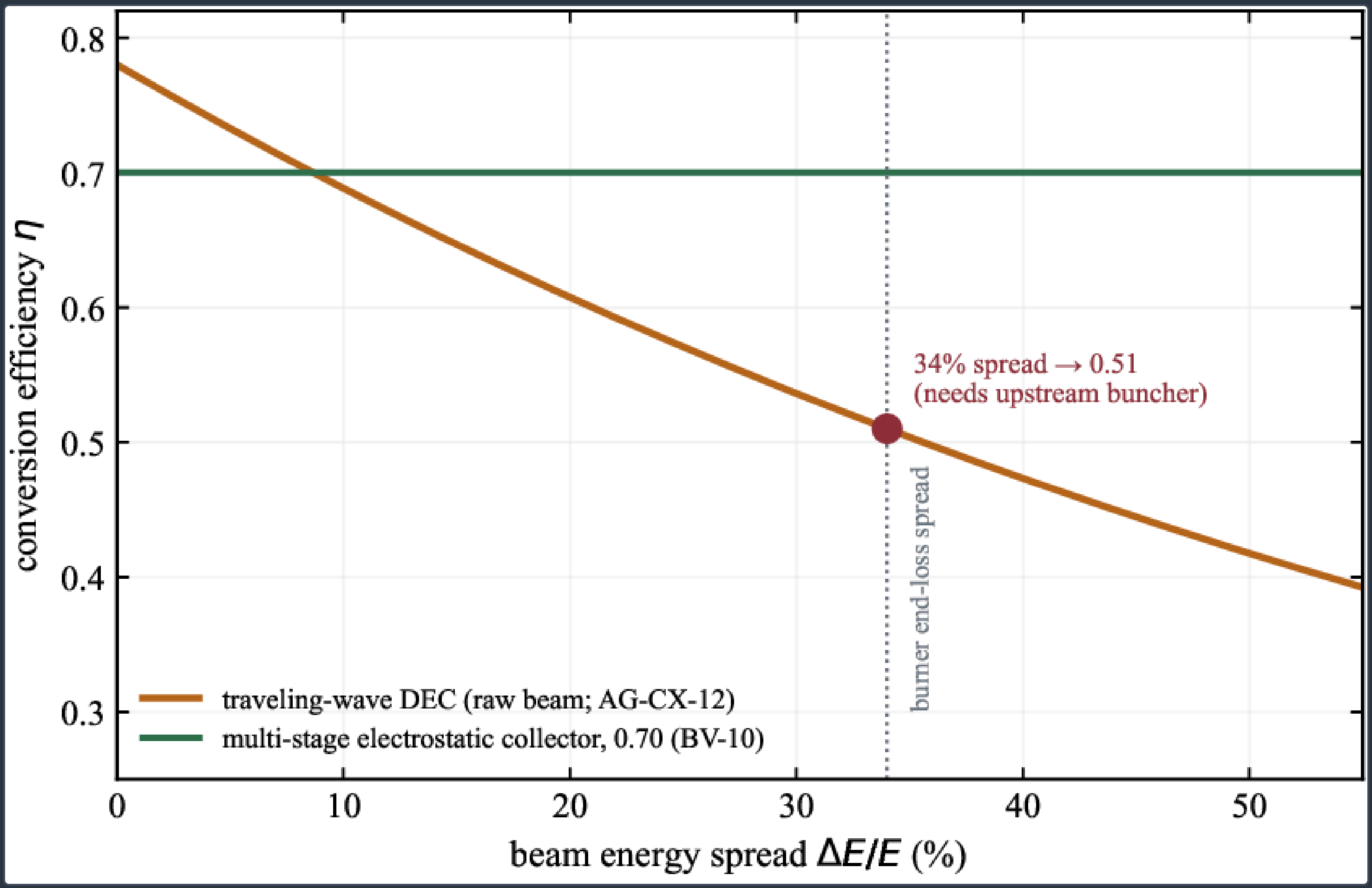

Traveling-wave versus multi-stage electrostatic collection against beam energy spread. The TWDEC (copper) degrades with un-bunched spread, reaching ∼**0.51** at the **34%** end-loss spread (AG-CX-12); the multi-stage electrostatic collector (green) holds the **0.70** design value because it sorts by energy (BV-10).

THE HVDC-NATIVE GRID INTERFACE

Because the collector produces high-voltage direct current, the converter is HVDC-native, and that reshapes the balance of plant electrically (figure 6; Table 1). Delivering power to the bus takes three conversion stages on the direct-DC path against five to six for a thermal plant's AC path (MV-L1-A3, MV-L1-A6). The isolation and step-down collapse into a single silicon-carbide dual-active-bridge stage optimised at 15.8 kHz with a 98.85% efficiency, and the direct path beats a solid-state-transformer-fed path by 3.0 points with one fewer stage (MV-CX-04). The gross HVDC-native delivery is 54.1% at $\phi_i = 248.7$ kV (MV-L1-A3). The cascade and the two grid paths are shown schematically in figures 9 and 10; the detailed load-side interface is developed in the companion interface paper [31] and the topology comparison in [32].

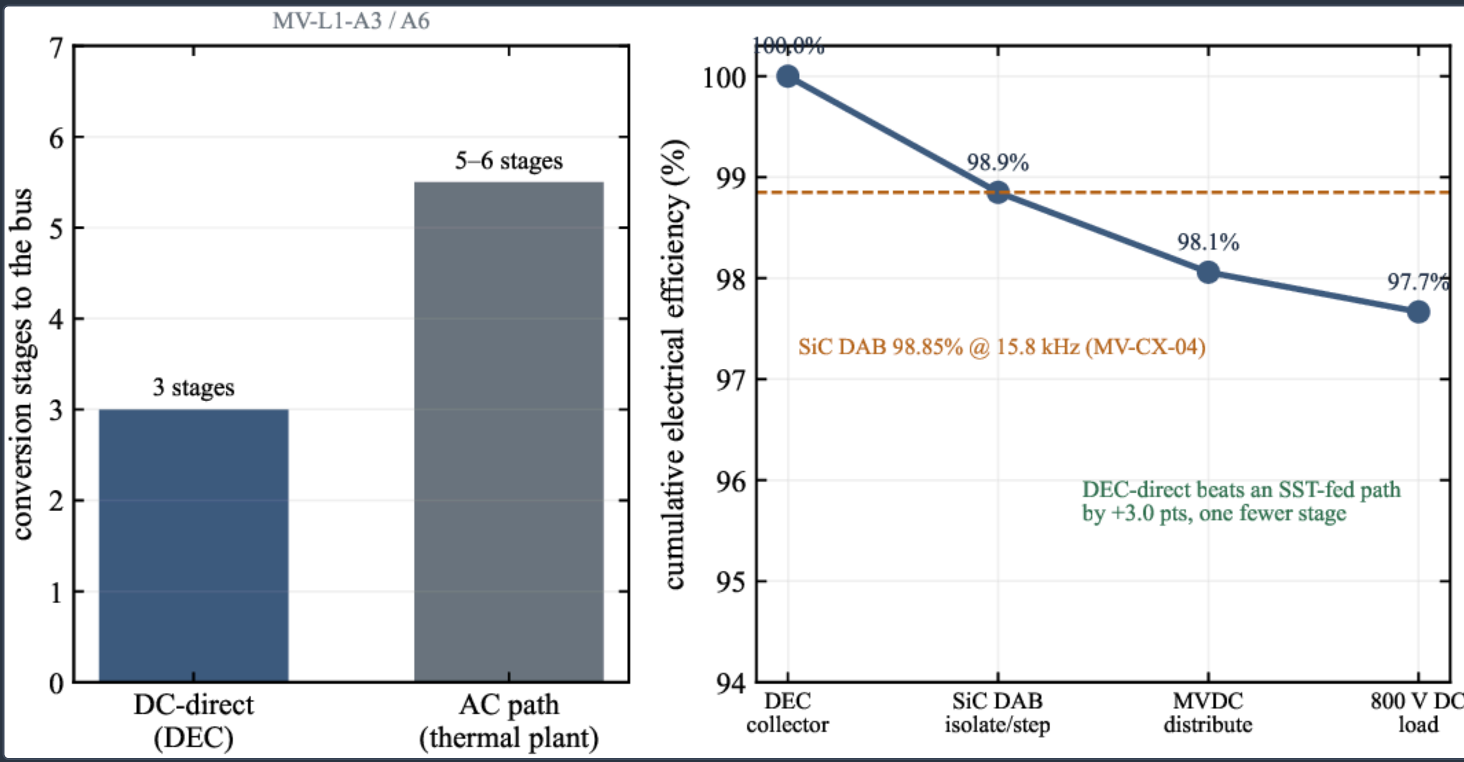

HVDC-native grid path. Left: conversion stages to the bus, three for the direct-DC (DEC) path against five to six for the AC path (MV-L1-A3/A6). Right: cumulative electrical efficiency down the direct-DC chain, with the frozen SiC dual-active-bridge stage at 98.85% (15.8 kHz; MV-CX-04); the direct path beats an SST-fed path by +3.0 points with one fewer stage.

DC POWER QUALITY: RIPPLE VERSUS HOLD-UP

Figure 7 shows the smoothing capacitance the DC output needs. Because the DEC output is inherently smooth, holding ripple to 1% needs only ~234 μF — far below the ~4.9 mF of hold-up that an IT load's ITIC ride-through already requires (MV-CX-03). The hold-up requirement dominates the capacitor bank, so no active harmonic filtering is needed; the DEC delivers clean DC by construction.

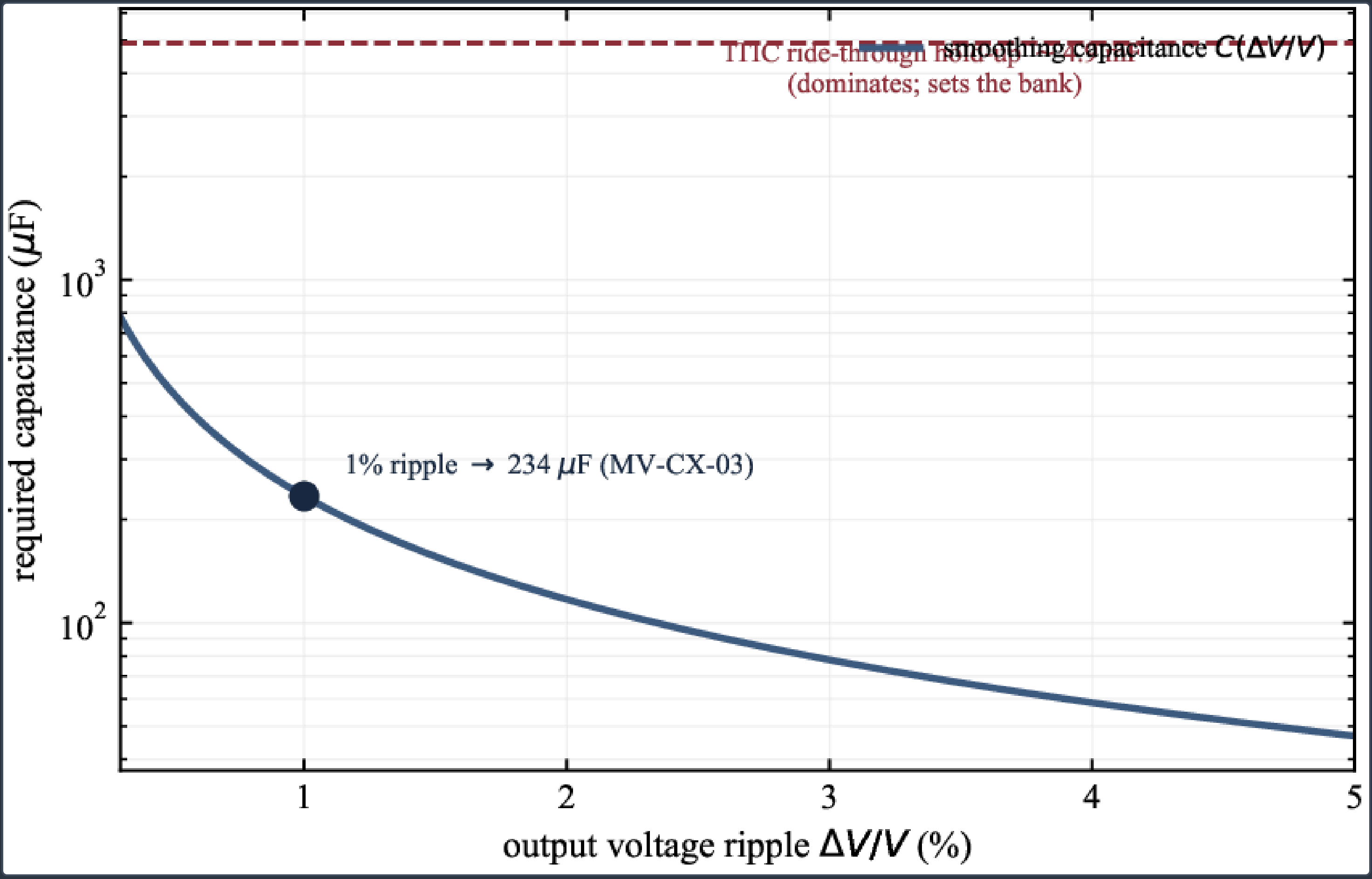

DC power quality. Smoothing capacitance versus output-voltage ripple; 1% ripple needs only ~234 μF (MV-CX-03), while ITIC ride-through hold-up (~4.9 mF, dashed) dominates the bank, so no active harmonic filtering is required.

THE ELECTRODE ALLOY

Figure 8 shows the DFT formation energies of the plasma-facing alloy family. The DEC electrode $W_{48}Ti_{33}Cr_{10}Ta_4V_4$ sits at −92 meV/atom (BR-SXD-01), negative like the first-wall and divertor alloys, so a single-phase BCC solid solution is favoured; the tantalum-free family brings the DEC electrode to a near-neutral −15 meV/atom (BR-L2-A37). The electrode is thus drawn from the same qualified low-activation refractory palette as the rest of the plasma-facing set [34,35,22,23,24], a composition-of-matter result rather than an off-the-shelf choice.

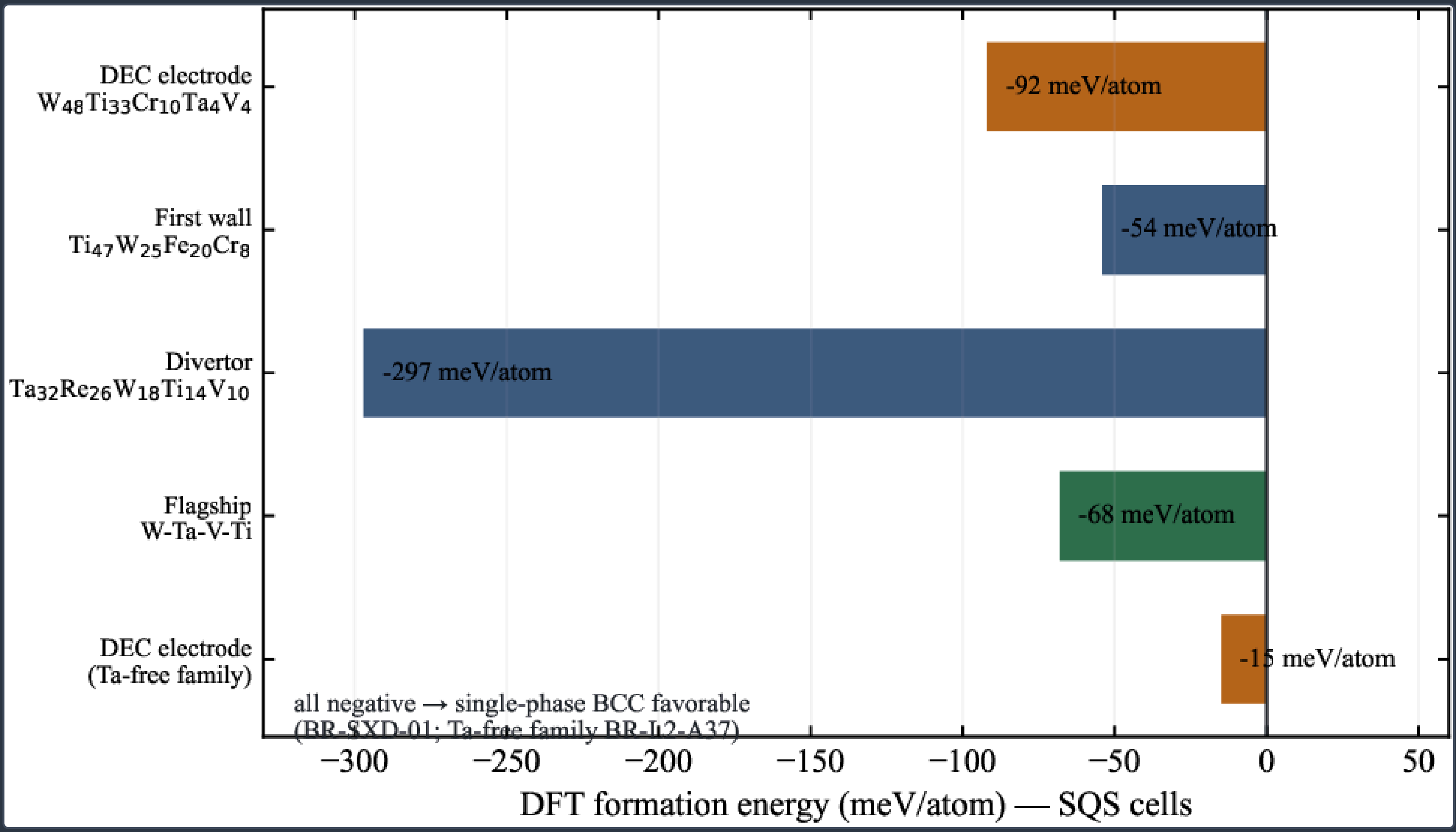

DFT formation energies (SQS cells) of the plasma-facing alloy family. The DEC electrode $W_{48}Ti_{33}Cr_{10}Ta_4V_4$ is −92 meV/atom (BR-SXD-01); the tantalum-free family reaches −15 meV/atom (BR-L2-A37). All values are negative, favouring a single-phase BCC solid solution.

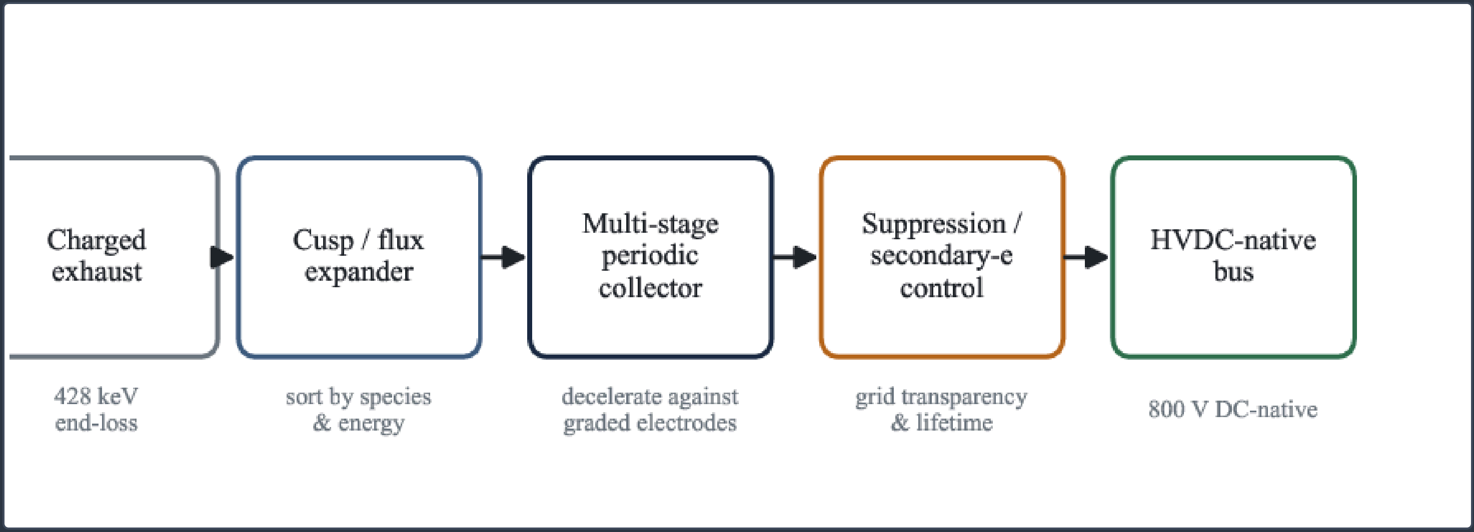

(Schematic.) The collector cascade: the 428 keV charged exhaust is expanded and sorted by species and energy, decelerated against the graded periodic collector, cleaned of back-streaming secondaries by a suppression stage, and delivered to the HVDC-native bus. No measured values are drawn.

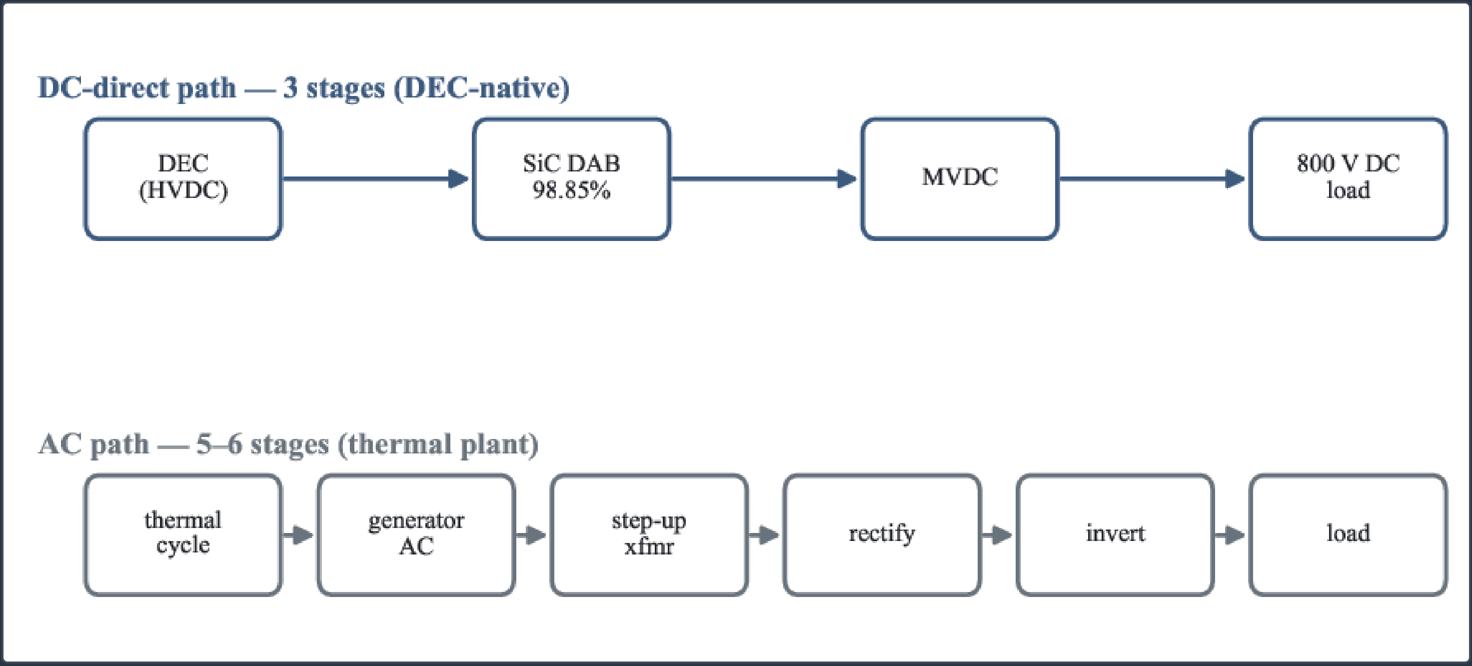

(Schematic.) Direct-DC versus AC grid paths. The DEC's native HVDC output reaches the load in three conversion stages through a single SiC dual-active-bridge; a thermal plant's AC output takes five to six. Stage counts are from MV-L1-A3/A6; the block diagram is illustrative.

QUANTITY	VALUE	SERIAL
end-loss spectrum, mean	$\bar{E} \simeq 428$ keV	BV-10
end-loss spectrum, fractional width	$\Delta E/E \simeq 34\%$	BV-10
central-cell escaping-ion band	253–513 keV	register
ion decelerating potential	$\phi_i = 248.7$ kV	MV-L1-A3
collector efficiency, 3 stages	$\eta_{\text{dec}} = 0.70$	BV-10
collector efficiency, 6 stages	$\eta_{\text{dec}} = 0.83$	BV-10
grid sub-efficiency	$\eta_{\text{grid}} = 0.93$	BV-10
graded implementation for design η	$\sim$10–13 stages	MV-CX-27
plant anchor (conservative)	$\eta = 0.49$	BU-SX-01
efficiency scope ladder	0.56 / 0.70 / 0.85	BU-SX-01/03, MV-SX-01
throttling robustness	$0.70 \to 0.687$ at 16% load	MV-CX-27
HVDC-native gross fraction	54.1%	MV-L1-A3
grid conversion stages, DC vs AC	3 vs 5–6	MV-L1-A3 / A6
SiC dual-active-bridge stage	98.85% at 15.8 kHz	MV-CX-04
DEC-direct advantage over SST path	+3.0 points, one fewer stage	MV-CX-04
DC ripple filter (1%)	$\sim$234 μF	MV-CX-03

table continued

ITIC ride-through hold-up	~4.9 mF	MV-CX-03
traveling-wave DEC at 34% spread	~51% (needs buncher)	AG-CX-12
electrode alloy	$W_{48}Ti_{33}Cr_{10}Ta_{4}V_{4}$	HX-19
electrode formation energy	−92 meV/atom	BR-SXD-01
electrode formation energy (Ta-free)	−15 meV/atom	BR-L2-A37

COMPUTATION	CODE	METHOD / DISCRETISATION	ANCHOR	
**collector gaps **	space charge	WarpX (LBNL) [13]	electrostatic PIC, CIC deposit, GPU multigrid Poisson	BV-10, MV-CX-27
electrode formation energy	Quantum ESPRESSO 7.3.1 [15,16]	plane-wave DFT (PBE), 16-atom SQS [17]	BR-SXD-01, BR-L2-A37	
**SiC DAB **	DC bus	switched transient circuit	single-phase-shift DAB, charge-balance sizing	MV-CX-04, MV-CX-03
grid stage count	topology analysis	cascaded-conversion count, DC vs AC	MV-L1-A3, MV-L1-A6	

The NVIDIA GPU-HPC campaign behind the results. No compute cost is reported.

§ 5

Discussion

THE COLLECTOR EFFICIENCY AGAINST THE PUBLISHED DEC RECORD

The classic Venetian-blind analysis of Moir and Barr projected collector efficiencies in the 0.7–0.9 range for mirror end-loss beams [4], and Barr's 100 kV beam-direct-converter experiments demonstrated recoveries consistent with that projection on real hardware [5]. Our result sits squarely inside that record: the module model reaches the Moir–Barr 0.70 design value at three stages and 0.83 at six over the *actual* 428 keV, 34%-wide spectrum, and the one-sided-quantiser structure of equations (2)–(5) makes the N-dependence a derived rather than an asserted curve. Where we differ from the classic treatment is in *deliberately anchoring below* the demonstrated value: the plant is frozen at 0.49, below the model floor of 0.56, so the power balance carries margin against the converter. This is the opposite of the historical tendency to quote a converter's best case, and it is the reason the burner's $Q_E = 1.318$ closure does not lean on the DEC.

THE SPACE-CHARGE AND EMISSION PHYSICS

Two effects that the idealised efficiency functional omits are exactly the ones the GPU-HPC campaign was built to resolve. The Child–Langmuir limit of equation (7) turns "grid transparency" from a free parameter into a hard constraint (8): the current a decelerating gap can pass scales as $\phi_i^{3/2}/d^2$, so a practical collector trades stage count and gap spacing against space-charge headroom, and this is why the robust graded design uses 10–13 stages rather than the three of the idealised module. Secondary electron emission, modelled with the probabilistic Furman–Pivi channels [14], debits the recovered current through equation (9); a suppression stage is therefore not optional but part of the cascade. Both are standard in the vacuum-electronics and accelerator literature; what is new here is folding them into a fusion DEC efficiency over a measured spectrum on a GPU-native PIC engine [13,10].

THE GRID INTERFACE AGAINST THE POWER-ELECTRONICS LITERATURE

The HVDC-native path is where direct conversion pays a second dividend. The single SiC dual-active-bridge stage at 98.85% is at the high end of what wide-bandgap devices and the dual-active-bridge topology deliver [18,19], and the direct path's advantage over a solid-state-transformer-fed alternative [20,21] — 3.0 points with one fewer conversion stage — follows directly from the DEC's output already being high-voltage DC, so the AC generation, step-up and rectification of a thermal plant are simply absent. The inherently smooth DC output, needing only $\sim 234\ \mu$F for 1% ripple against ~ 4.9 mF of load-mandated hold-up, means the converter is a clean DC source by construction. For a DC-native load such as a data centre or a forward-base microgrid this is a structural, not incremental, advantage [36,31,32].

MATERIALS CONSISTENCY

The electrode is not a separate materials problem. Its formation energy of -92 meV/atom (BR-SXD-01), and the near-neutral -15 meV/atom of the tantalum-free family (BR-L2-A37), place it in the same first-principles low-activation refractory high-entropy family as the first wall and divertor [34,35,22,23], screened to avoid the long-lived activation tail [24]. The converter is therefore materials-consistent with the machine it serves, and its electrode is a composition-of-matter result of the same DFT campaign, not an off-the-shelf choice.

RELATION TO THE DISPATCH AND CONTROL LAYER

The collector does not run open-loop. Its potentials, suppression bias and dispatch are commanded by the burner's real-time control suite — the DEC dispatch and efficiency optimiser, the direct-converter collector optimiser, the end-loss-ion recovery optimiser and the two-species expander controller [37] — which hold the electrode placement near the optimum of equation (5) as the spectrum drifts, and which are what make the throttling robustness of figure 4 an operational property rather than a static one.

§ 6

Limitations

The collector efficiencies reported here are validated at module level in simulation — an electrostatic PIC model of a single periodic cell over the measured spectrum, with the space-charge and secondary-emission physics resolved — and cross-checked against the published Venetian-blind and beam-direct-converter record [4,5]. The one open confirming measurement is a collector-prototype beam bench that recovers the staircase efficiency on real hardware at the burner's potential and current density; until that bench exists, the plant is deliberately anchored at $\eta = 0.49$, below the model floor of 0.56, so that the design carries margin against the converter rather than depending on its best case. This is a single, honest gate, and it does not move the frozen anchors.

§ 7

Conclusion

The Kronos burner's direct energy converter is efficient and grid-friendly at the frozen operating point, and both properties are now derived rather than asserted. Casting the multi-stage collector as a one-sided energy quantiser of the 428 keV end-loss spectrum, subject to the Child–Langmuir space-charge limit on every gap and a Furman–Pivi secondary-emission debit, yields an electrode-placement optimality condition whose staircase efficiency matches the frozen module result: $\eta_{\mathrm{dec}} = 0.70$ at three stages and 0.83 at six, with an $\eta_{\mathrm{grid}} = 0.93$ sub-efficiency, on a scope ladder anchored conservatively at 0.49 and topping out at an ideal 0.85. The efficiency holds under a six-fold turndown ($0.70 \rightarrow 0.687$), a traveling-wave converter is inferior on the raw 34% spread ($\sim 51\%$), and the HVDC-native output reaches the bus in three stages with a 98.85% SiC dual-active-bridge stage and needs only $\sim 234\ \mu$F of filtering. The electrodes are a near-neutral, low-activation refractory alloy from the same qualified palette as the rest of the plasma-facing set. Direct conversion is both the efficient and the electrically simpler way to take power off this machine, and the plant is built to carry margin against it.

Acknowledgments tocsectionAcknowledgments Part of the Kronos Fusion Energy 2026 design series. The authors thank the Kronos physics and computing teams for the de-risking campaign and its independent gate re-runs.

Reproducibility. The collector-efficiency ladder, spectrum, throttling, traveling-wave, grid-interface, ripple and electrode values are frozen results (BV-10, AG-CX-12, MV-CX-27, MV-CX-04, MV-CX-03, MV-L1-A3, MV-L1-A6, BU-SX-01, BU-SX-03, MV-SX-01, HX-19, BR-SXD-01, BR-L2-A37) in the Kronos Physics De-Risking Register, doi:10.5281/zenodo.22133057. The collector PIC model (WarpX), the electrode density-functional outputs (Quantum ESPRESSO 7.3.1) and the power-electronics transient model are regenerable from the archived inputs; the figure scripts in this deposit reproduce every panel from the frozen anchors and from the first-principles Child–Langmuir evaluation. This paper is archived at doi:10.5281/zenodo.22645858 and its official version is hosted at https://www.kronosfusionenergy.com/publications/direct-energy-converter-collector-physics-in-a-d-he-tan.html.

Data availability tocsectionData availability This paper is archived at doi:10.5281/zenodo.22645858. The collector-model, power-electronics and DFT inputs and the figure scripts are archived with the deposit and reference the Kronos 2026 series and its Physics De-Risking Register, doi:10.5281/zenodo.22133057. Any economic analysis is reported separately and is not included in the public deposit.

Competing interests tocsectionCompeting interests Provisional patent applications relating to aspects of this work, including the direct-energy-converter electrode composition of matter, have been filed. The authors declare no other competing interests.

tocsectionReferences

APPARATUS

Portfolio, People & Record

The intellectual-property estate, the people who built it, the limitations that gate it, and the sources it rests on.

1	4	40	27
GRANTED PATENT	2026 PROVISIONALS	TEAM MEMBERS	2022 PROVISIONALS

INTELLECTUAL PROPERTY

The patent portfolio

The estate spans a granted high-field magnet patent, pending utility and 2026 provisional filings that map to the two products, a digital-twin control provisional, a registered trademark application, and the original 2022 provisional family. Every patentable disclosure in the five-paper arXiv drop was protected **before** publication: the breeder and burner provisionals were filed 1–2 August, and a publication-gap omnibus filing the evening before the drop swept up the DEC, plasma-control, and REBCO-winding matter of the three otherwise-unprotected papers. Patent numbers and application serials are matters of public record; claim scope is summarised, not reproduced.

GRANTED & PENDING UTILITY

US 12,009,112	High-field tilted graded-REBCO magnet architecture (KRONO-002A) · *app. 17/878,550*	GRANTED
US 17/878,507	Core device / method (KRONO-001A) · *utility*	PENDING

2026 PROVISIONAL FILINGS — MAPPED TO THE PRODUCTS

64/124,209	Hyperion — spherical-tokamak tritium / helium-3 foundry · *breeder · filed Aug 2026*	FILED
64/124,220	Aegis / MetroVolt — synchrotron-cutoff, fuel-selection & plug-winding · *generator · filed Aug 2026*	FILED
64/115,167	KRONOS-CTRL digital-twin plant control · *provisional · filed Jul 2026*	FILED
64/005,440	Integrated spherical-tokamak fusion architecture · *early integrated-architecture filing · filed Mar 2026*	FILED
64/105,530	Negative-triangularity spherical-tokamak architecture · *foundational ST filing · filed Jul 2026*	FILED
64/128,097	Publication-gap omnibus — quasineutral two-species expander DEC · provenance-gated / latency-split plasma control · as-built high-field winding & conductor architecture · *filed 7 Aug 2026, the evening before the arXiv drop*	FILED

TRADEMARK & ORIGIN

FTK-98801894	Kronos Fusion Energy — trademark application	FILED
KR-2022-*	Original provisional family (KR-2022-00001 … 00027) · *27 filings, 2022*	PRIORITY

The narrow, defensible magnet novelty — the specific conductor and the digital-twin winding optimisation, not high-field REBCO as a category — is the commercial core that can earn ahead of any Q > 1 milestone, with markets in fusion magnet supply, MRI/NMR, accelerators, and proton therapy. The claim is scoped honestly: the high field is a *system field* result, not a stand-alone-coil record; the small-bore plug coil is structurally infeasible as a bare winding but resolved by a stress-managed structural shield (feasible-pending-FEA); and the winding-tape experiment returned a *null result*. The value is the method, not a field record.

THE TEAM

Founding partners, board, advisors & auditors

Kronos is built by a bench of advanced-fuel-fusion, high-field-magnet, direct-conversion, and materials specialists, with a board and operations team drawn from defense, national laboratories, and industry. Dates are shown as ranges; where a tenure has ended or is term-ending, the range says so.

FOUNDING PARTNERS — SCIENCE

Dr. Gerald Kulcinski
Co-Founder · Helium-3 & Advanced-Fuel Fusion
UW–Madison · 2023–Present

Dr. Carl Weggel
Chief Scientist / S.M.A.R.T. Design
MIT Alcator Program · 2022–Present

Dr. Robert J. Weggel
Magnetic Field Design
MIT Magnet Lab · 2022–Present

BOARD

Priyanca Ford
Founder & CEO · Executive Board
2022–Present

Bandel Carano
Finance / Strategy
Oak Investment Partners / Stanford · 2025–2026

Patrick Schweiger
Fusion Device Engineering
Oklo / CFS / TerraPower · 2025–Present

SCIENTIFIC ADVISORS

Dr. Steven O. Dean
Fusion Policy & History
DOE / Fusion Power Associates · 2025–Present

Dr. Patrick H. Diamond
Plasma Turbulence & Transport
UC San Diego · 2025–Present

Dr. Jack J. Dongarra
HPC & Numerical Algorithms
Turing Award · 2025–Present

Dr. Nasr M. Ghoniem
Chief Material Scientist
UCLA · 2025–Present

Dr. Siegfried Glenzer
Plasma Physics & Laser Fusion
Stanford / SLAC · 2022–Present

Dr. David A. Hammer
Pulsed-Power Fusion
Cornell · 2025–Present

Dr. Donald A. Spong
Plasma Theory & Confinement
ORNL · 2025–Present

Dr. Curtis Smith
Risk Assessment & Nuclear PRA
MIT / Idaho National Lab · 2025–Present

RADM (Ret.) David Goggins
Naval Engineering & Power-Plant Design
U.S. Navy · 2023–2026

Dr. Konstantin Batygin
Mathematician
Caltech · 2022–2025

Dr. Ruben Fair
Magnet Design / ITER Liaison
PPPL / Jefferson Lab · 2022–2025

Dr. Paul S. Weiss
Materials & Nanotechnology
UCLA · 2022–2025

SCIENTIFIC AUDITORS

Dr. Wilfred A. Cooper
Plasma Equilibrium Theory
EPFL / Swiss Plasma Center · 2025–Present

Dr. Ahmed Hassanein
Plasma–Material Interactions
Purdue / Argonne · 2025–Present

Dr. Patrick E. Hopkins
Extreme Thermal Materials
U. of Virginia · 2025–Present

Dr. Peter Hosemann
Materials Joining & Structural Integrity
UC Berkeley · 2025–Present

Dr. Travis W. Knight
Advanced Nuclear Fuels & Systems
U. of South Carolina · 2025–Present

Dr. Philippe Lebrun
Cryogenics & Magnet Cooling
CERN · 2025–Present

Dr. Nitendra Singh
Nuclear Safety & Fuel Cycle
ITER · 2025–Present

Dr. Guido Van Oost
Magnetic Confinement & Fusion Systems
Ghent University · 2025–Present

Dr. Gary S. Was
Radiation Materials & Structural Integrity
U. of Michigan · 2025–Present

Dr. Ray Sedwick
Direct Energy Conversion
U. of Maryland · 2025

OPERATIONS

Michael Laughlin
Chief Operating Officer
2022–Present

Martin Owens
Chief Strategy Officer
LANL / GE Hitachi · 2022–Present

MG (Ret.) Paul Pardew
Chief Contracting Officer
Army Contracting Command · 2022–Present

David Beck
Fusion Commercialization
U.S. Space Force · 2024–Present

Sushma Bhatia
Environmental & Legislative
Google · 2022–Present

Michael De Frenza
Technology Licensing
2023–Present

MG (Ret.) Robin L. Fontes
Cybersecurity & Defense
Army Cyber Command · 2022–Present

Vijay Gehani
Supply Chain & Components
INOX India · 2024–Present

Jon Michel Greenwood
IT & AI Infrastructure
Live Nation · 2023–Present

Brian C. O'Neill
National Security
CIA / ODNI · 2022–Present

Gen. (Ret.) Gustave F. Perna
DoD Liaison
Operation Warp Speed · 2022–2023

Andrea Romero
Marketing Lead
2022–Present

Legal counsel is retained; those roles are held on the internal roster and are not listed here.

SOURCES

References

1 W M Nevins, A review of confinement requirements for advanced fuels, *J. Fusion Energy* **17** 25 (1998). doi:10.1023/A:1022513215080

2 L M Hively, A simple computational form for Maxwellian reactivities, *Nucl. Technol.–Fusion* **3** 199 (1983). doi:10.13182/FST83-A20840

3 R F Post, The magnetic mirror approach to fusion, *Nucl. Fusion* **27** 1579 (1987). doi:10.1088/0029-5515/27/10/001

4 R W Moir and W L Barr, “Venetian-blind” direct energy converter for fusion reactors, *Nucl. Fusion* **13** 35 (1973). doi:10.1088/0029-5515/13/1/005

5 W L Barr, R W Moir and G W Hamilton, Experimental results from a beam direct converter at 100 kV, *J. Fusion Energy* **2** 131 (1982). doi:10.1007/BF01054580

6 D Endrizzi *et al*, Physics basis for the Wisconsin HTS Axisymmetric Mirror (WHAM), *J. Plasma Phys.* **89** 975890501 (2023). doi:10.1017/S0022377823000806

7 C D Child, Discharge from hot CaO, *Phys. Rev. (Series I)* **32** 492 (1911).

8 I Langmuir, The effect of space charge and residual gases on thermionic currents in high vacuum, *Phys. Rev.* **2** 450 (1913).

9 C K Birdsall and A B Langdon, *Plasma Physics via Computer Simulation* (Adam Hilger/IOP Publishing, Bristol, 1991).

10 J P Verboncoeur, Particle simulation of plasmas: review and advances, *Plasma Phys. Control. Fusion* **47** A231 (2005). doi:10.1088/0741-3335/47/5A/017

11 S P Lloyd, Least squares quantization in PCM, *IEEE Trans. Inf. Theory* **28** 129 (1982). doi:10.1109/TIT.1982.1056489

12 J Max, Quantizing for minimum distortion, *IRE Trans. Inf. Theory* **6** 7 (1960). doi:10.1109/TIT.1960.1057548

13 L Fedeli *et al*, Pushing the frontier in the design of laser-based electron accelerators with groundbreaking mesh-refined particle-in-cell simulations on exascale-class supercomputers, in *SC22: Int. Conf. for High Performance Computing, Networking, Storage and Analysis* (2022) 1. doi:10.1109/SC41404.2022.00008

14 M A Furman and M T F Pivi, Probabilistic model for the simulation of secondary electron emission, *Phys. Rev. ST Accel. Beams* **5** 124404 (2002). doi:10.1103/PhysRevSTAB.5.124404

15 P Giannozzi *et al*, QUANTUM ESPRESSO: a modular and open-source software project for quantum simulations of materials, *J. Phys.: Condens. Matter* **21** 395502 (2009). doi:10.1088/0953-8984/21/39/395502

16 P Giannozzi *et al*, Advanced capabilities for materials modelling with Quantum ESPRESSO, *J. Phys.: Condens. Matter* **29** 465901 (2017). doi:10.1088/1361-648X/aa8f79

17 A Zunger, S-H Wei, L G Ferreira and J E Bernard, Special quasirandom structures, *Phys. Rev. Lett.* **65** 353 (1990). doi:10.1103/PhysRevLett.65.353

18 R W A A De Doncker, D M Divan and M H Kheraluwala, A three-phase soft-switched high-power-density DC/DC converter for high-power applications, *IEEE Trans. Ind. Appl.* **27** 63 (1991). doi:10.1109/28.67533

19 J Mill\'an, P Godignon, X Perpi\ n\`a, A P\'erez-Tom\'as and J Rebollo, A survey of wide bandgap power semiconductor devices, *IEEE Trans. Power Electron.* **29** 2155 (2014). doi:10.1109/TPEL.2013.2268900

20 X She, A Q Huang and R Burgos, Review of solid-state transformer technologies and their application in power distribution systems, *IEEE J. Emerg. Sel. Topics Power Electron.* **1** 186 (2013). doi:10.1109/JESTPE.2013.2277917

21 S Debnath, J Qin, B Bahrani, M Saeedifard and P Barbosa, Operation, control, and applications of the modular multilevel converter: a review, *IEEE Trans. Power Electron.* **30** 37 (2015). doi:10.1109/TPEL.2014.2309937

22 O N Senkov, G B Wilks, D B Miracle, C P Chuang and P K Liaw, Refractory high-entropy alloys, *Intermetallics* **18** 1758 (2010). doi:10.1016/j.intermet.2010.05.014

23 E P George, D Raabe and R O Ritchie, High-entropy alloys, *Nat. Rev. Mater.* **4** 515 (2019). doi:10.1038/s41578-019-0121-4

COLOPHON

How this document was made

The Kronos Fleet — Combined Editorial, 2026 is set in **Fraunces** (display), **Gelasio** (text), and **IBM Plex Mono** (data & equations), carried forward from the Kronos editorial design system.

The figures are rendered at 300 dpi from the deposited generator scripts; the document is composed as a single self-contained file with embedded fonts and imagery, paginated to US Letter, and rendered to PDF through a headless Chromium engine in matched light and dark editions.

Every headline quantity carries an evidence class; withdrawn and restated values are marked as such. Nothing herein is frozen beyond the founder-approved Tier-A set.

Explore it live — turn the interactive 3-D model, run the deposited solvers in the physics validator, and watch the companion film series.

◆

LEGAL NOTICE

Notice, status, and distribution

Conceptual design & simulation study. This document reports a conceptual design and simulation study. It is not a construction commitment, a safety-analysis report, a regulatory filing, or an offer of securities. Forward-looking statements — schedules, costs, market sizes, and performance — are estimates subject to the limitations set out in the Simulations part and may change.

Numbers and their classes. Quantities are reported with evidence classes and case labels; modelled, assumed, and requirement-class values are identified as such and are not to be quoted without their labels.

Public edition. This edition carries the physics and design only; all financial, funding, and defense-commercial content has been removed for public distribution. The scientific text corresponds to the arXiv and journal submissions.

THE 2026 KRONOS SERIES

One programme, many papers

This editorial is one paper in the Kronos 2026 series — a real fusion company's complete, reproducible physics record for a spherical-tokamak breeder and its low-neutron D–^{3}He tandem-mirror burners. Every headline number is a frozen anchor in the Physics De-Risking Register.

Explore the whole programme: the De-Risking Register, the interactive 3-D model, and the physics validator.

KRONOS FUSION ENERGY

Direct-Energy-Converter Collector Physics in a D-^{3}He Tandem-Mirror Burner: Multi-Stage Deceleration, Secondary Emission, and the Space-Charge-Limited Grid Optimum

A real fusion company building real machines. Explore the science, live.

Zenodo · doi:10.5281/zenodo.22645858

Read on kronosfusionenergy.com

The Physics De-Risking Register